

# Open Materials Generation with Stochastic Interpolants

Philipp Höllmer,<sup>1,2,\*</sup> Thomas Egg,<sup>1,2,\*</sup> Maya M. Martirosyan,<sup>1,2,\*</sup> Eric Fuemmeler,<sup>3,\*</sup> Amit Gupta,<sup>3</sup> Zeren Shui,<sup>4</sup> Pawan Prakash,<sup>5</sup> Adrian Roitberg,<sup>6,7</sup> Mingjie Liu,<sup>6,7</sup> George Karypis,<sup>4</sup> Mark Transtrum,<sup>8</sup> Richard G. Hennig,<sup>9,7</sup> Ellad B. Tadmor,<sup>3</sup> and Stefano Martiniani<sup>1,2,10,11</sup>

<sup>1</sup>Center for Soft Matter Research, Department of Physics, New York University, New York 10003, USA

<sup>2</sup>Simons Center for Computational Physical Chemistry, Department of Chemistry, New York University, New York 10003, USA

<sup>3</sup>Department of Aerospace Engineering and Mechanics, University of Minnesota, Minneapolis, MN 55455, USA

<sup>4</sup>Department of Computer Science & Engineering, University of Minnesota, Minneapolis, MN 55455, USA

<sup>5</sup>Department of Physics, University of Florida, Gainesville, FL 32611, USA

<sup>6</sup>Department of Chemistry, University of Florida, Gainesville, FL 32611, USA

<sup>7</sup>Quantum Theory Project, University of Florida, Gainesville, FL 32611, USA

<sup>8</sup>Department of Physics & Astronomy, Brigham Young University, Provo, UT 84602, USA

<sup>9</sup>Department of Materials Science & Engineering, University of Florida, Gainesville, FL 32611, USA

<sup>10</sup>Courant Institute of Mathematical Sciences, New York University, New York 10003, USA

<sup>11</sup>Center for Neural Science, New York University, New York 10003, USA

The discovery of new materials is essential for enabling technological advancements. Computational approaches for predicting novel materials must effectively learn the manifold of stable crystal structures within an infinite design space. We introduce Open Materials Generation (OMG), a unifying framework for the generative design and discovery of inorganic crystalline materials. OMG employs stochastic interpolants (SI) to bridge an arbitrary base distribution to the target distribution of inorganic crystals via a broad class of tunable stochastic processes, encompassing both diffusion models and flow matching as special cases. In this work, we adapt the SI framework by integrating an equivariant graph representation of crystal structures and extending it to account for periodic boundary conditions in unit cell representations. Additionally, we couple the SI flow over spatial coordinates and lattice vectors with discrete flow matching for atomic species. We benchmark OMG’s performance on two tasks: Crystal Structure Prediction (CSP) for specified compositions, and *de novo* generation (DNG) aimed at discovering stable, novel, and unique structures. In our ground-up implementation of OMG, we refine and extend both CSP and DNG metrics compared to previous works. OMG establishes a new state-of-the-art in generative modeling for materials discovery, outperforming purely flow-based and diffusion-based implementations. These results underscore the importance of designing flexible deep learning frameworks to accelerate progress in materials science.

## I. INTRODUCTION

A core objective of materials science is the discovery of new synthesizable structures and compounds with the potential to meet critical societal demands. The development of new materials such as room-temperature superconductors [1], high-performance alloys with exceptional mechanical properties [2–4], advanced catalysts [5, 6], and materials for energy storage and generation [7, 8] hold the potential to drive technological revolutions.

Exploring the vast compositional and structural landscape of multicomponent materials with novel properties is essential, yet exhaustive experimental screening is infeasible [9]. Quantum and classical molecular simulation offer a powerful alternative, enabling a more targeted and efficient exploration. In recent decades, both experimental [10, 11] and computational [12, 13] high-throughput pipelines have led to a proliferation of materials databases for crystal structures [14, 15] and simulations [16–18]. These advances have already facilitated the development of more accurate machine-learned interatomic potentials [19–21].

Still, efficiently sampling the manifold of stable materials structures under diverse constraints—such as composition and target properties—remains a major challenge. Traditional approaches to materials discovery have relied on first-principles electronic structure methods such as DFT—or more sophisticated theory, depending on the property [22–24]—which, while powerful and fairly accurate, are very computationally expensive. These methods include *ab initio* random structure searching (AIRSS) [25] or genetic algorithms for structure and phase prediction [26], both of which have successfully predicted new crystal structures and some of which have even been experimentally realized [27]. However, the high computational cost of these approaches has limited the scope and speed of material exploration, highlighting the need for cutting-edge ML techniques to significantly accelerate the discovery of stable inorganic crystalline materials.

### A. Related works

Recent advances in machine learning techniques have generated significant interest in applying data-driven approaches for inorganic materials discovery. Among these, Graph Networks for Materials Exploration (GNoME) has

\* These authors contributed equally.

demonstrated remarkable success by coupling coarse sampling strategies for structure and composition with AIRSS that leverages a highly accurate machine-learned interatomic potential (MLIP) to predict material stability, leading to the identification of millions of new candidate crystal structures [28]. Other frameworks have approached the generation of composition and structure jointly through fully ML-based methods. Crystal Diffusion Variational Autoencoder (CDVAE) leverages variational autoencoders and a graph neural network representation to sample new crystal structures from a learned latent space [29]. To date, state-of-the-art performance in both crystal structure prediction for given compositions and *de novo* generation of novel stable materials has been achieved by diffusion models such as DiffCSP [30] and MatterGen [31], as well as conditional flow-matching frameworks such as FlowMM [32].

While these approaches have demonstrated that ML can push the boundaries of computational materials discovery, it remains uncertain whether score-based diffusion or flow-matching represent the definitive methodological frameworks for this problem. Furthermore, the extent to which the optimal approach depends on the training data remains an open question. Thus far, each new method has typically outperformed its predecessors across datasets.

## B. Our contribution

The work we present in this paper is the first implementation and extension of the stochastic interpolants (SIs) framework [33] for the modeling and generation of inorganic crystalline materials. SIs are a unifying framework that encompasses both flow-based and diffusion-based methods as specific instances, while offering a more general and flexible framework for generative modeling. In this context, SIs define a stochastic process that interpolates between pairs of samples from a known base distribution and a target distribution of inorganic crystals. By learning the drift terms of either ordinary differential equations (ODEs) or stochastic differential equations (SDEs), new samples can be generated by numerically integrating these equations. The flexibility of the SI framework stems from the ability to tailor the choice of interpolants, and the incorporation of an additional random latent variable, further enhancing its expressivity. With their many degrees of freedom, SIs thus provide an ideal framework for optimizing generative models for materials design.

We implement the SI framework in the open-source Open Materials Generation (OMG) package, released alongside this paper. OMG allows to train and benchmark models for two materials generation tasks: *Crystal structure prediction* (CSP) which only learns to generate atomic positions and lattice vectors for a given composition, and *de novo generation* (DNG) which learns to generate both crystal structure and composition to predict novel materials. We discover that optimizing interpolation schemes for different degrees of freedom—particularly fractional

coordinates in the crystal representation—substantially improves performance across diverse datasets. As a result, our approach achieves a new state of the art—outperforming both DiffCSP [30] and FlowMM [32]—in CSP and DNG across all evaluated datasets for both existing, revised, and new performance measures.

## II. BACKGROUND

### A. Diffusion models

A widely used approach in generative modeling uses diffusion models [34], which define a stochastic process that progressively transforms structured data into noise. A model is then trained to approximate the reverse process, enabling the generation of new samples. These models are often formulated in terms of SDEs, where the forward process follows a predefined diffusion dynamic.

Score-based diffusion models (SBDMs) are an instantiation of diffusion models that learn a score function—the gradient of the log probability density—to guide the reversal of the diffusion process via numerical integration [35]. SBDMs have demonstrated remarkable success in generating high-quality and novel samples across a wide range of applications where the target distribution is complex and intractable, such as photorealistic image generation [36] and molecular conformation prediction [37].

### B. Conditional flow matching

Conditional flow matching (CFM) [38] is a generative modeling technique that learns a flow which transports samples from a base distribution at time  $t = 0$  to a target distribution at time  $t = 1$ . This process defines a probability path that describes how samples are distributed at any intermediate time  $t \in [0, 1]$ . The velocity field associated with this flow governs how individual samples evolve over time. CFM learns the velocity indirectly by constructing conditional vector fields that are known *a priori*. Once trained, samples drawn from the base distribution can be evolved numerically to generate new samples from the target distribution. Originally, CFM was formulated using Gaussian conditional probability paths, but Tong *et al.* [39] later extended this framework to allow for arbitrary probability paths and couplings between base and target distributions. A further extension, particularly relevant to physics and chemistry, is Riemannian flow matching (RFM), which generalizes CFM to Riemannian manifolds [40]. This allows in particular to use the flow-matching framework for systems with periodic boundary conditions as they appear in unit cell representations of inorganic crystals [32].

### III. OPEN MATERIALS GENERATION

#### A. Stochastic Interpolants

SIs provide a unifying mathematical framework for generative modeling, generalizing both SBDMs and CFM [33]. The SI  $x(t, x_0, x_1, z)$  bridges the base distribution  $\rho_0$  with a target distribution  $\rho_1$  by learning a time-dependent drift  $b^\theta(t, x)$ . In this work, we focus on stochastic interpolants between  $\rho_0$  and  $\rho_1$  of the form:

$$x_t \equiv x(t, x_0, x_1, z) = \alpha(t)x_0 + \beta(t)x_1 + \gamma(t)z. \quad (1)$$

Here,  $t \in [0, 1]$  represents time and  $(x_0, x_1)$  are paired samples drawn from  $\rho_0$  and  $\rho_1$ , respectively. The random variable  $z$  is drawn from a standard Gaussian  $\mathcal{N}(0, \mathbf{I})$  independently of  $x_0$  and  $x_1$ . The functional forms of  $\alpha$ ,  $\beta$ , and  $\gamma$  are flexible, subject to few constraints (see Appendix A 2). The inclusion of the latent variable  $\gamma(t)z$  allows sampling of an ensemble of paths around the mean interpolant  $I(t, x) = \alpha(t)x_0 + \beta(t)x_1$ , and is theorized to improve generative modeling by promoting smoother and more regular learned flows [33].

For generative modeling, it is most important that the time-dependent density  $\rho(t)$  of the stochastic process  $x_t$  in Eq. 1 can also be realized either *via* deterministic sampling through an ODE (derived from a transport equation) or stochastic sampling through an SDE (derived from a Fokker–Planck equation) only requiring  $x_0 \sim \rho_0$  (see Appendix A 1). For both ODE- and SDE-based sampling, the required drift term  $b^\theta(t, x) : [0, 1] \times \mathbb{R}^d \rightarrow \mathbb{R}^d$  is learned by minimizing the loss function

$$\mathcal{L}_b(\theta) = \mathbb{E}_{t,z,x_0,x_1} [ |b^\theta(t, x_t)|^2 - 2 \partial_t x(t, x_0, x_1, z) \cdot b^\theta(t, x_t) ], \quad (2)$$

where the expectation is taken independently over  $t \sim \mathcal{U}(0, 1)$  with  $\mathcal{U}(0, 1)$  the uniform distribution between 0 and 1,  $z \sim \mathcal{N}(0, \mathbf{I})$ ,  $x_0 \sim \rho_0$ , and  $x_1 \sim \rho_1$ . For SDE-based sampling, an additional denoiser  $z^\theta(t, x) : [0, 1] \times \mathbb{R}^d \rightarrow \mathbb{R}^d$  must be learned by minimizing an additional loss

$$\mathcal{L}_z^\theta(\theta) = \mathbb{E}_{t,z,x_0,x_1} [ |z^\theta(t, x_t)|^2 - 2 z^\theta(t, x_t) \cdot z ]. \quad (3)$$

The drift term, along with the denoiser in the case of SDE-based sampling, enables the generation of samples from the target distribution [33]. For ODE-based sampling,  $\gamma(t) = 0$  is a possible choice. For SDE-based sampling, however,  $\gamma(t) > 0$  is required for all  $t \in (0, 1)$  (see Appendix A 1).

By appropriately selecting interpolation functions  $\alpha$ ,  $\beta$ ,  $\gamma$  and choosing between deterministic (ODE) and stochastic (SDE) sampling schemes, the SI framework not only recovers CFM and SBDM as special cases but also enables the design of a broad class of novel generative models (see Appendix A 2 for examples). The strength of OMG’s SI implementation for materials discovery lies in its ability to tune both the interpolation and sampling schemes, as illustrated in Fig. 1 for a pair of structures sampled from

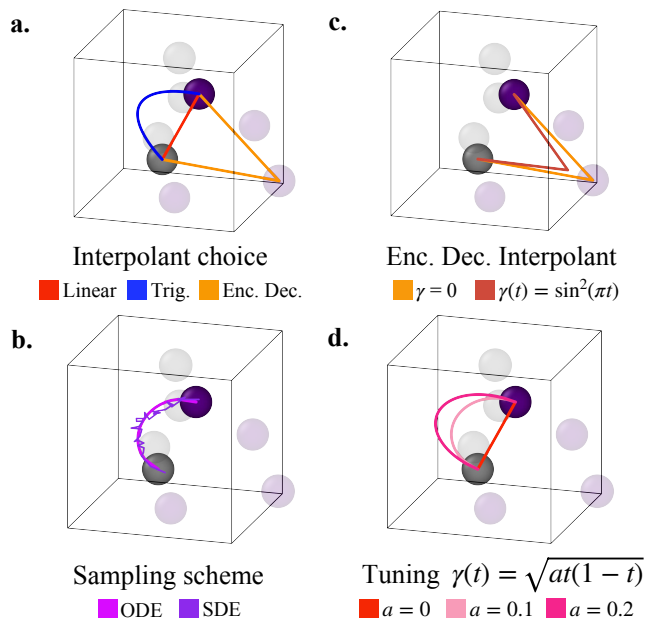


FIG. 1. Visualization of the tunable components of the SI framework for bridging samples  $x_0$  (gray particles) and  $x_1$  (purple particles). (a) The choice of the interpolant changes the path of the time-dependent interpolation trajectory. (b) During inference, the learned drift term  $b^\theta(t, x)$  and denoiser  $z^\theta(t, x)$  generate new samples via standard ODE or SDE integration, here for a linear interpolant with  $\gamma = \sqrt{0.07t(1-t)}$ . (c) The inclusion of a latent variable  $\gamma(t)z$  changes the interpolation path. (d) The function  $\gamma(t, a) = \sqrt{at(1-t)}$  depends on  $a$  that also influences the interpolation path.

$\rho_0$  and  $\rho_1$ . By systematically optimizing over this large design space, we achieve superior performance for CSP and DNG tasks across datasets, as discussed in Section V.

#### B. Crystal representation and generation

A crystalline material is defined by its idealized repeat unit, or unit cell, which encodes its periodicity. In the OMG representation, a unit cell is described by separating the material’s chemical composition—given by its atomic species  $\mathbf{A} \in \mathbb{Z}_{>0}^N$ , where  $N$  is the number of atoms in the unit cell—from its structural representation—its fractional coordinates  $\mathbf{X} \in [0, 1]^{3 \times N}$  with periodic boundaries and lattice vectors  $\mathbf{L} \in \mathbb{R}^{3 \times 3}$ . During training, all three components  $\{\mathbf{A}, \mathbf{X}, \mathbf{L}\}$  are considered simultaneously. We apply the SI framework only to the continuous structural representations  $\{\mathbf{X}, \mathbf{L}\}$  with loss functions defined in Eq. 2 and 3, and use discrete flow matching (DFM) on the chemical species  $\mathbf{A}$  [41]. The number of atoms  $N$  in the structure  $x_0$  sampled from the base distribution  $\rho_0$  is determined by the number of atoms in the corresponding structure  $x_1$  sampled from the target distribution  $\rho_1$ .

### 1. Atomic coordinates

We specify the base distribution for the fractional coordinates  $\mathbf{x} \in [0, 1)$  for all  $\mathbf{x} \in \mathbf{X}$  via a uniform distribution (except for the score-based diffusion interpolant that requires a wrapped normal distribution  $\rho_0(\mathbf{x})$  following the approach of Jiao *et al.* [30]; see Section IV A). For learning fractional coordinates, we implement a variety of periodic interpolants that connect the base to the target data distributions. To satisfy periodic boundary conditions on the paths defined by the interpolants, we extend the SI framework to the surface of a four-dimensional torus in this paper. Reminiscent of RFM [40], the linear interpolant on the torus traverses a path equivalent to the shortest-path geodesic which is always<sup>1</sup> well-defined. Other interpolants, however, are more complex. In order to uniquely define them, we always define the interpolation with respect to the shortest-path geodesic. That is, for interpolation between  $\mathbf{x}_0$  and  $\mathbf{x}_1$  with a periodic boundary at 0 and 1, we first unwrap  $\mathbf{x}_1$  to the periodic image  $\mathbf{x}'_1$  which has the shortest possible distance from  $\mathbf{x}_0$ . Following this, the interpolation between  $\mathbf{x}_0$  and  $\mathbf{x}'_1$  is computed given a choice of interpolant, and the traversed path is wrapped back into the boundary from 0 to 1. This approach is illustrated in Appendix A 4.

### 2. Lattice vectors

To construct the base distribution for the cell vectors  $\mathbf{L}$ , we follow Miller *et al.* [32] and use an informed log-normal distribution  $\rho_0(\mathbf{L})$  which is fitted to the distribution of cell vectors in each target dataset. This leverages the flexibility in the SI framework to choose arbitrary base distributions in contrast to SBDM which necessarily requires a Gaussian base distribution.

### 3. Atomic species

The discrete nature of chemical compositions  $\mathbf{A}$  in atomic crystals requires a specialized approach for generative modeling. To address this, we implement discrete flow matching (DFM) [42]. In our implementation of the DFM framework, each atomic species  $\mathbf{a} \in \mathbf{A}$  can take values in  $\{1, 2, \dots, 100\} \cup \{M\}$ ; where  $\{1 - 100\}$  are atomic element numbers and  $M$  is a masking token used during training. The base distribution is defined as  $\rho_0(\mathbf{a}) = [M]^N$ , meaning that initially all  $N$  atoms are masked. As sampling progresses, the identities of the atoms evolve *via* a continuous-time Markov Chain (CTMC), and are progressively unmasked to reveal valid

atomic species. At  $t = 1$ , all masked tokens are replaced. To learn this process, we define a conditional flow  $p_{t|1}(\mathbf{a}_t|\mathbf{a}_1)$  that linearly interpolates in time from the fully masked state  $\mathbf{a}_0$  toward  $\mathbf{a}_1$  and thus yields the composition  $\mathbf{a}_t$  of the interpolated structure  $x_t$ . Based on these conditional flows, a neural network is trained to approximate the denoising distribution  $p_{1|t}^\theta(\mathbf{a}_1|x_t)$ , which yields the probability for the composition  $\mathbf{a}_1$  given the entire structure  $x_t$ , by minimizing a cross-entropy loss

$$\mathcal{L}_{\text{DFM}}(\theta) = \mathbb{E}_{t, x_1, x_t} \left[ \log p_{1|t}^\theta(\mathbf{a}_1|x_t) \right]. \quad (4)$$

In doing this, we are able to directly construct the marginal rate matrix  $R_t^\theta(\mathbf{a}_t, i)$  for the CTMC that dictates the evolution of  $\mathbf{a}_t$  at time  $t$  to the next time step during generation (see Appendix A 5). It is important to note that the learned probability path is a function of the entire atomic configuration  $\{\mathbf{A}, \mathbf{X}, \mathbf{L}\}$  which is necessary for the prediction of chemical composition from structure.

### C. Joint generation with stochastic interpolants

For both CSP and DNG tasks, we seek to generate samples from a joint distribution over multiple coordinates. For DNG, this joint distribution  $\rho_1$  encompasses all elements of a crystal unit cell. For CSP we similarly model the joint distribution,  $\rho_1$ , but with atom types fixed to compositions sampled from the target dataset. For both tasks, the total loss function is formulated as a weighted sum of the individual loss functions for each variable (see Appendix B 2), and their relative weights are optimized (see Appendix B 3). We illustrate both types of models and their structure generation process in Fig. 2.

Additionally, for DNG, we consider a two-step process in which composition is learned separately from structure, as seen in Fig. 2b. In this approach, we first train a Chemical Formula Prediction (CFP) model (see Appendix B 1) to generate compositions optimized for SMACT stability [43], similarity in the distribution of  $N$ -arity of known structures, as well as uniqueness and novelty. The predicted compositions are then used as input for a pre-trained CSP model, which generates the corresponding atomic configurations.

### D. Data-dependent coupling

SIs have been used with data-dependent couplings [44], where a coupling function  $\nu(x_0, x_1)$  enables biasing of  $x_0$  based on the sampled  $x_1$ . In OMG, we incorporate an optional data-dependent coupling that enforces an ordering (*i.e.*, a permutation on the order of atomic elements within a structure) that produces the minimum fractional-coordinate distance between each particle pair  $(\mathbf{x}_0^i, \mathbf{x}_1^i)$  from structures  $x_0 \in \rho_0$  and  $x_1 \in \rho_1$  (see Appendix A 6). We find that the inclusion of this data-dependent coupling is optimal during hyperparameter tuning depending on

<sup>1</sup> The only exception being when two points are precisely half the box length apart. However, this case is not relevant for the given base distribution.

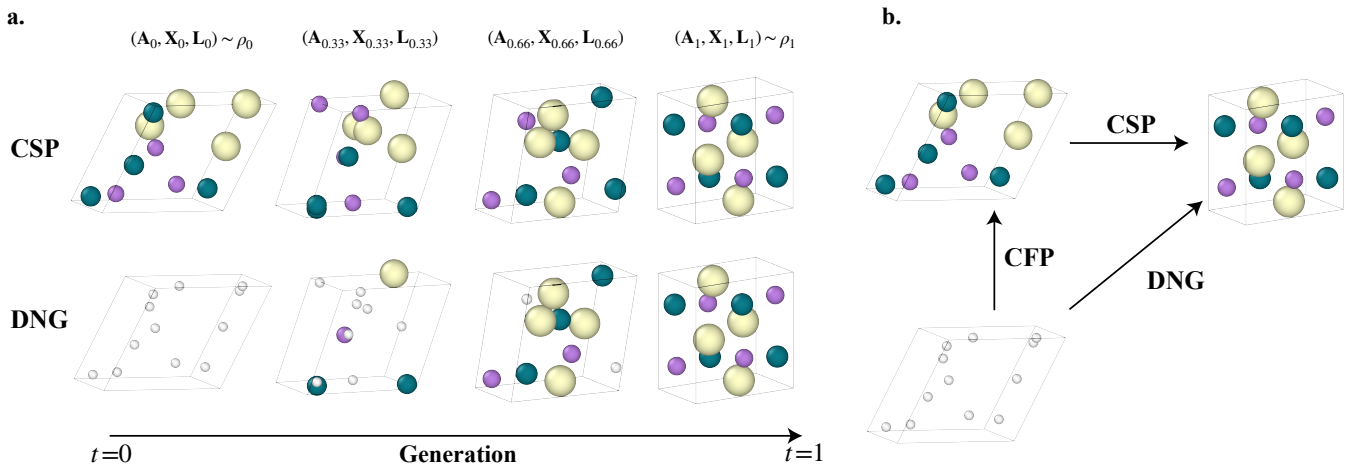


FIG. 2. Illustration of CSP and DNG tasks. (a) For CSP, the species  $\mathbf{A}$  are fixed with known compositions from  $t = 0$ . From this, we predict  $\mathbf{X}$  and  $\mathbf{L}$  from randomly sampled initial values. For DNG, we predict  $(\mathbf{A}, \mathbf{X}, \mathbf{L})$  jointly. Our implementation of DFM initializes  $\mathbf{A}$  as a sequence of masked particles that are unmasked through a series of discrete jumps to reveal a physically reasonable composition. (b) Two avenues for performing *de novo* generation of materials. The first uses two steps: a CFP model predicts compositions and then uses a CSP model to find accompanying stable structures. The second trains a DNG model over cell, species, and fractional coordinates jointly as shown in (a).

the type of model: CSP models typically performed better without this coupling, but DNG models (see Tab. IV) can benefit in certain cases from minimizing traveled distance *via* permutation of elements.

### E. Velocity annealing

Velocity annealing—rescaling the learned drift during generation to increase velocity over time as  $b^\theta(t, x) \rightarrow (1 + st)b^\theta(t, x)$  with  $s$  as an hyperparameter during integration—has been empirically shown to improve performance in a number of studies that apply CFM to physical systems [32, 45, 46]. For instance, Miller *et al.* [32] demonstrated that applying velocity annealing significantly improves performance in CSP and DNG benchmarks for materials. Motivated by these findings, we include velocity annealing in OMG as a tunable hyperparameter, while emphasizing that this technique lacks a formal theoretical justification within the mathematical frameworks underlying flow models and stochastic interpolants.

## IV. METHODOLOGY

### A. Choice of interpolant

In training OMG, we optimize the choice of the interpolating function that is used during training. Albergo *et al.* [33] introduced four interpolants of the form defined in Eq. 1, each shaping the interpolation trajectory differently (see also Appendix A 2 for further details).

The **linear** interpolant defines a constant velocity trajectory from  $x_0$  to  $x_1$ . When combined with an ODE sampling scheme and  $\gamma = 0$ , this reproduces a particular choice of CFM. If the sampling scheme or  $\gamma$  is changed, however, the use of linear interpolants become distinct from CFM. The **trigonometric** interpolant prescribes trajectories with more curvature than the linear interpolant. The **encoder-decoder** interpolant first evolves samples from  $\rho_0$  to follow an intermediate standard Gaussian distribution  $\mathcal{N}(0, \mathbf{I})$  at time  $t = 0.5$ , before mapping them to  $\rho_1$  at  $t = 1$ . This approach has been found to interpolate more smoothly between distributions, potentially mitigating the formation of spurious features in the probability path at intermediate times [33]. Lastly, we consider the variance preserving **score-based diffusion (SBD)** interpolant. When paired with an SDE sampling scheme, this interpolant is mathematically equivalent to an SBDM, but on the continuous time interval  $[0, 1]$ . The SBD interpolant assumes that  $\rho_0$  is a Gaussian, and unlike the previous three interpolants it involves no explicit latent variable; instead the  $\alpha(t)x_0$  term takes on this role. We note that the trajectory of the encoder-decoder interpolant between times  $t = 0.5$  and  $t = 1$  resembles that of the SBD interpolant between times  $t = 0$  and  $t = 1$ . For the example of using the encoder-decoder interpolant only for the coordinates, however, we emphasize that the Gaussian-distributed coordinates at  $t = 0.5$  are conditioned on other coordinates that are halfway-interpolated at this point. Conversely, for SBD interpolation, the Gaussian distributed coordinates at  $t = 0$  are only conditioned on other random variables since, at this point, all elements of  $x_0$  are randomly distributed.

We prioritize flexibility in learning the atomic coordinates,  $\mathbf{X}$ , as our findings indicate that learning drifts

TABLE I. Results from crystal structure prediction. Match rate and RMSE of matched structures without (left) and with (right) filtering for structural and compositional validity are reported for all models. For OMG’s model, the choice of positional interpolant, latent variable component  $\gamma$ , and sampling scheme are noted.

Method	<i>perov-5</i>		<i>MP-20</i>		<i>MPTS-52</i>		<i>Alex-MP-20</i>	
	Match (%) $\uparrow$	RMSE $\downarrow$	Match (%) $\uparrow$	RMSE $\downarrow$	Match (%) $\uparrow$	RMSE $\downarrow$	Match (%) $\uparrow$	RMSE $\downarrow$
DiffCSP	53.08/51.94	<b>0.0774/0.0775</b>	57.82/52.51	<b>0.0627/0.0600</b>	15.79/14.29	<b>0.1533/0.1489</b>	-	-
FlowMM	53.63/51.86	0.1025/0.0994	66.22/59.98	0.0661/0.0629	22.29/20.28	0.1541/ <b>0.1486</b>	-	-
OMG	<b>80.85/79.55</b>	0.3864/0.3873	<b>69.83/63.75</b>	0.0741/0.0720	<b>27.38/25.15</b>	0.1970/0.1931	<b>69.44/61.38</b>	<b>0.1303/0.1289</b>
	Trig; ODE; $\gamma = \sqrt{0.113t(t-1)}$		Linear; ODE; $\gamma = 0$		Linear; ODE; $\gamma = 0$		Linear; ODE; $\gamma = 0$	

and denoisers which generate the positional distribution with high fidelity are more difficult than for the other two coordinates of interest. As such, we evaluate the periodic versions of the four interpolants outlined above on learning the generation of atomic positions  $\mathbf{X}$ , but only use the linear interpolant with  $\gamma = 0$  for the lattice vectors  $\mathbf{L}$ .

## B. Equivariant representation of crystal structures

Imposing inductive biases on the latent representation of the crystal structure can promote data efficiency and improve learning. The CSPNet architecture [30], originally adopted in DiffCSP, is an equivariant graph neural network (EGNN) [47] that produces a permutation- and rotation-equivariant, as well as translation-invariant representation of the crystal structures.

In the current OMG implementation, we employ CSPNet as an encoder that is trained from scratch. The CSPNet architecture encodes atomic types using learnable atomic embeddings and represents fractional coordinates through sinusoidal positional encodings (see Appendix B1). These features are processed through six layers of message-passing, after which the encoder produces the drift  $b^\theta(t, x)$  of both the lattice and the fractional coordinates, as well as potentially predicting the denoiser  $z^\theta(t, x)$ . For DNG, the network must also predict  $\log p_{1|t}^\theta(\mathbf{a}_1|x_t)$ . The resulting outputs inherently preserve the permutation, rotational, and translational symmetries embedded in CSPNet.

The output of CSPNet is invariant with respect to translations of the fractional coordinates in the input. Thus, one should, in principle, use a representation of the fractional coordinates that does not contain any information about translations. While this is straightforward in Euclidean space by removing the mean of the coordinates of the given structure, this cannot be done with periodic boundary conditions where the mean is not uniquely defined. We follow Miller *et al.* [32] and instead remove the center-of-mass motion when computing the ground-truth  $\partial_t x(t, x_0, x_1, z)$  in Eq. 2.

Alternative EGNNs such as NequIP [19], M3GNet [21], or MACE [20] which have been widely used for the development of MLIPs can also serve as plug-and-play encoders

within OMG’s SI framework. Integrating different architectures is a direction that we plan to explore in future iterations of the framework.

## C. Comparison to other frameworks

We report results for the CSP task in Tab. I and for the DNG task in Tabs. II and III for DiffCSP, FlowMM, and OMG. We detail in Sec. V how we improve the extant benchmarks used in the field and therefore recompute all CSP and DNG benchmarks. In nearly all cases, we were able to generate structures using the DiffCSP and FlowMM source code which closely matched (within  $\sim 1\%$ ) the previously reported metrics in their respective manuscripts. The observed differences can be attributed to the use of a newer version of SMACT composition rules<sup>2</sup> [43] and to natural fluctuations arising from model retraining.

Since the focus of this work is to assess our model’s ability to learn unconstrained and unconditioned flows, we do not compare against symmetry-constrained generation methods [48–52]. Symmetry constraints can be incorporated in future extensions of the flexible OMG framework.

## V. EXPERIMENTS

### A. Benchmarks and datasets

We use the following datasets to benchmark the OMG model: *perov-5* [54], a dataset of perovskites with 18,928 samples with five atoms per unit cell in which only lattice lengths and atomic types change; *MP-20* [29, 55] from the Materials Project that contains 45,231 structures with a maximum of  $N = 20$  atoms per unit cell, and *MPTS-52* [56] which is a time split of the Materials Project with 40,476 structures with up to  $N = 52$  atoms per unit cell and is typically the most difficult to learn.

<sup>2</sup> The SMACT Python library updated its default oxidation states with the release of version 3.0.

TABLE II. Results from *de novo* generation of 10,000 structures with models trained on the MP-20 dataset. The integration steps for OMG is chosen based on best overall performance. For DiffCSP and FlowMM, we recomputed all metrics. All OMG models in this table use the ODE sampling scheme. Best scores in each category are bolded.<sup>a</sup>

Method	Integration steps	Validity (% $\uparrow$ )			Coverage (% $\uparrow$ )			Property ( $\downarrow$ )	
		Structural	Composition	Combined	Recall	Precision	wdist ( $\rho$ )	wdist ( $N$ -ary)	wdist ( $\langle CN \rangle$ )
DiffCSP	1000	99.91	82.68	82.65	<b>99.67</b>	99.63	0.3133	0.3193	0.3053
FlowMM	1000	92.26	83.11	76.94	99.34	99.02	1.0712	0.1130	0.4405
OMG									
Linear; $\gamma = 0$	150	99.64	<b>87.02</b>	<b>86.77</b>	99.39	<b>99.86</b>	0.0834	0.0784	<b>0.1371</b>
Trig; $\gamma = \sqrt{1.19t(1-t)}$	690	97.89	<b>85.74</b>	<b>83.97</b>	98.51	<b>99.83</b>	<b>0.0646</b>	0.1914	<b>0.1806</b>
Enc-Dec; $\gamma = \sin^2 \pi t$	840	97.25	<b>86.35</b>	<b>84.19</b>	99.62	99.61	0.1155	<b>0.0553</b>	<b>0.0465</b>
SBDM; $\gamma = 0$	690	96.38	<b>84.19</b>	81.14	98.94	<b>99.80</b>	0.0788	0.1287	<b>0.1127</b>
CFP + CSP (Linear, $\gamma = 0$ )	130+210	97.95	79.68	78.21	<b>99.67</b>	99.50	0.5614	0.2008	0.6256

<sup>a</sup> We do not bold any values in the structural validity category as the CDVAE model reports the state-of-the-art with 100% structural validity. For the Wasserstein density and  $N$ -ary metrics, we only bold values lower than 0.075 and 0.079 respectively, as these were the values reported by FlowMM for their model with 500 integration steps (not included in this table).

TABLE III. Stability, uniqueness, and novelty results from *de novo* generation on the MP-20 dataset computed for the same models as in Tab. II. All evaluations are performed with the MatterGen code base [53] with respect to the included reference *Alex-MP-20* dataset. The average RMSD is between the generated and the relaxed structures, and the average energy above hull is reported in units of eV/atom. <sup>a</sup>

Method	$\langle E \rangle / N$ ( $\downarrow$ ) above hull	RMSD ( $\text{\AA}$ , $\downarrow$ )	Stability (% $\uparrow$ )	S.U.N. (% $\uparrow$ )
			Rate	Rate
DiffCSP	0.1984	1.295	43.04	19.00
FlowMM	0.2509	0.651	37.47	13.86
OMG				
Linear	<b>0.1438</b>	<b>0.294</b>	<b>69.11</b>	18.58
Trig	<b>0.1842</b>	0.763	<b>49.49</b>	<b>19.12</b>
Enc-Dec	<b>0.1699</b>	<b>0.390</b>	<b>58.56</b>	17.59
SBDM	0.2215	0.759	41.04	<b>20.16</b>
CFP + CSP	0.2340	<b>0.488</b>	42.21	<b>20.50</b>

<sup>a</sup> OMG’s performance is comparable to the 22.56% S.U.N. Rate and 0.11 $\text{\AA}$  RMSD reported by the MatterGen-MP model when trained on *MP-20* [31], though we cannot directly compare to these benchmarks as those structures are relaxed using DFT.

We use the same 60-20-20 splits as Xie *et al.* [29], Jiao *et al.* [30], Miller *et al.* [32]. For the *Alex-MP-20* dataset [31], we used an 80-10-10 split constructed from MatterGen’s 90-10 split, in which we removed 10% of the training data to create a test dataset. This dataset contains 675,204 structures with 20 or fewer atoms per unit cell from the *Alexandria* [57, 58] and *MP-20* datasets. We do not include the *carbon-24* dataset [59] in our results, as match rate is ill-defined for this dataset; because all elements are carbon, it is not clear how many generated structures are unique and producing a structure that matches one in the reference dataset is trivial<sup>3</sup>.

<sup>3</sup> Previous papers [29, 30, 32] report match rate for *carbon-24*, but they do not compare the generated structure to the entirety of the reference dataset; their results suggest the match tolerance is larger than the differences between the *carbon-24* structures.

## B. Performance metrics

We assess the state-of-the-art performance of OMG’s models using a variety of standard, refined, and contributed benchmarks. For CSP (see Tab. I), the match rate and root mean square distance (RMSD) of matched structures are computed between the test dataset and the generated structures using Pymatgen’s `StructureMatcher` module [60] with tolerances (`stol = 0.5`, `ltol = 0.3`, `angletol = 10`).

For DNG (see Tab. II), metrics include validity (structural and compositional), coverage (recall and precision), and Wasserstein distances between distributions of properties including density  $\rho$ , number of unique elements  $N$  (*i.e.*, an  $N$ -ary material), and average coordination number by structure  $\langle CN \rangle$ . We introduce the average coordination number benchmark in part due to the difficulty of generating symmetric structures; a structure’s average coordination number is a useful fingerprint, and higher-coordinated structures tend to be more symmetric.

The previous DNG metrics are used during optimization of hyperparameters (see Appendix B 3), with the best models on the validation set being used to calculate stability rate as well as the S.U.N. (stable, unique, and novel) rate (see Tab. III). The stability-based metrics are calculated using MatterGen’s code base [53], in which the machine-learned interatomic potential MatterSim [61] is utilized for structural relaxation. This requires significantly less compute time in comparison to running DFT relaxations. For all models with reported S.U.N. rates, we generated a set of 10,000 structures which are filtered to remove those with elements not handled by MatterSim. Further details are provided in Appendix C. In addition to the stability and S.U.N. rates, we also provide in Tab. II the average RMSD between the generated and relaxed structures, as well as the average energy above the convex hull. Figure 3 compares the histograms of the energies above hull of the generated structures between OMG, DiffCSP, and FlowMM, and shows OMG’s superior performance for the generation of stable structures.

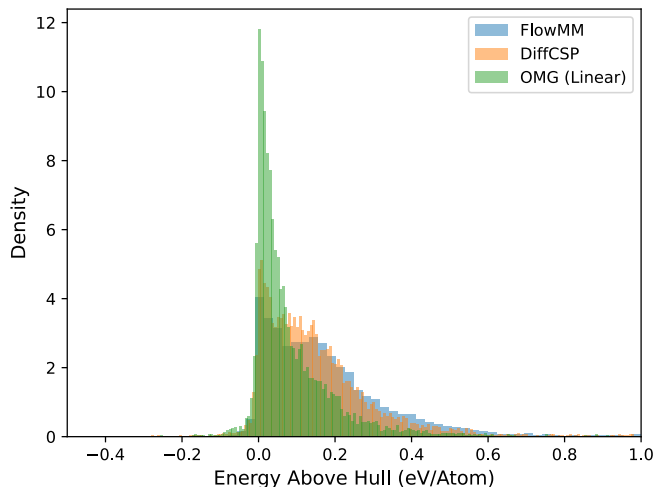


FIG. 3. Histogram of the computed energies above the convex hull for structures generated by FlowMM, DiffCSP, and OMG (linear interpolant). The OMG model consistently produces lower energy structures compared to FlowMM and DiffCSP. See Appendix C 3 for calculation details.

We have refined the calculation of several metrics, and reported these for all models. Previously reported match rates filtered the matched generated structures by their validity according to structural constraints on interatomic distances  $r > 0.5\text{\AA}$  as well as SMACT composition rules [43] which screen structures by their electron valence and charge neutrality. We note, however, that the datasets themselves contain invalid structures—for example, the *MP-20* test dataset has  $\sim 10\%$  compositionally invalid structures. Thus, we argue that the removal of these invalid structures for computation of match rate and RMSE is not reasonable for assessing learning performance; we do, however, provide both match rates (with and without validation filtering).

## VI. DISCUSSION AND CONCLUSIONS

During hyperparameter optimization for CSP models, we observed a tradeoff between match rate and RMSE—which is only computed if matched—between the ideal and generated crystals. By adjusting the relative cost between the position, cell, and species terms in the loss, we observe that the main learning challenge lies in the accurate prediction of the atomic coordinates, which always have a significantly higher relative weight in calculating the full loss function in Eq. B7 in the appendix. Unsurprisingly, we find that as the number of generated structures matching known compositions in the test dataset increases, the structural fidelity of these matches—quantified by the accompanying RMSE—also tends to increase. We quantify this tradeoff in Fig. 7 in the appendix. However, match rate remains the primary metric of interest, as the generated structure can always be relaxed after generation if seeking minimum energy structures (i.e., at zero

temperature).

For the CSP task, OMG significantly outperforms previous approaches on all datasets. We highlight the particularly strong performance of the trigonometric interpolant in achieving a high match rate for the *perov-5* dataset as shown in Tab. I. Unlike other datasets, *perov-5* has a fixed number of atoms  $N$  per unit cell and a fixed (cubic) cell with varying side lengths and identical fractional positions. In contrast, in other datasets, *no unique representation of the periodic repeat unit is imposed on flows*, meaning the model does not learn the invariance (or even equivariance) to the choice of periodic repeat unit.<sup>4</sup> This likely contributes to the difficulty of unconstrained flow-based models in generating highly symmetric structures. The *perov-5* dataset presents a unique case where this invariance does not need to be learned, making it an ideal benchmark for evaluating which positional interpolant can best learn structural relationship when the species are fixed. The match rate achieved using the trigonometric interpolant in Tab. I surpasses (by  $1.6\times$ ) our best-performing linear interpolant model for *perov-5*, which has a lower match rate of 51.86% (without filtering invalid atoms) and an RMSE of 0.0757 (state-of-the-art for this metric). It is possible that the superior performance of the trigonometric interpolant arises from its ability to generate more circuitous flow trajectories compared to the strictly geodesic paths imposed by the linear interpolant, akin to the reasoning behind using latent variables to enhance learning in SIs [33].

Finally, we note trends in Tab. IV among the best-performing models identified through hyperparameter optimization. In particular, we observe a tradeoff between the choice of positional interpolant and the optimal level of ‘species noise’  $\eta$  which sets the probability that an atom will change its identity if already in an unmasked state (see Appendix A 5), with linear interpolants favoring higher species noise. Additionally, we find a correlation between enabling element order permutation (to minimize the distance between  $x_0$  and  $x_1$ ) and the use of geodesic (linear) interpolation paths, with linear interpolants favoring minimum distance permutation. Therefore, we conclude that DNG models built on linear interpolants likely benefit from targeted tuning strategies that are unnecessary for non-geodesic positional interpolants.

In conclusion, we demonstrate OMG’s capabilities for learning the manifold of stable materials and generating novel structures. We show state-of-the-art performance of SIs across nearly all benchmarks for both crystal structure prediction as well as *de novo* generation of stable, novel, and unique structures. In our discussion, we highlight several ways in which hyperparameters and interpolation paths influence learning, though a more systematic theoretical analysis is needed to fully understand why specific

<sup>4</sup> Using Niggli reduction during learning to enforce a unique choice of unit cell on structures from our datasets is not sufficient for enforcing this invariance during generation of structures.

TABLE IV. Optimally performing DNG trials from OMG. All models are trained with an ODE sampling scheme and ordered by decreasing species noise  $\eta$ . The values of whether the element ordering is permuted to minimize traveled distance is also included.

Positional Interpolant	Min. dist. permutation	Species noise
Linear, $\gamma = 0$	True	35.46
Linear, $\gamma = 0$	True	31.29
Linear, $\gamma = 0$	True	7.08
SBD, $\gamma = 0$	False	1.95
EncDec, $\gamma = \sin^2 \pi t$	False	0.85
Trig, $\gamma = \sqrt{1.19t(1-t)}$	True	0.81

choices affect model performance. Future work can also extend the flexibility of OMG to additional interpolating functions. We underscore the importance of flexible ML frameworks like OMG, which can adapt to different types of materials datasets by optimizing the generative model

accordingly. Our work represents a key step forward in applications of machine-learning methods to materials discovery.

## VII. ACKNOWLEDGEMENTS

This work was supported in part through the NYU IT High Performance Computing resources, services, and staff expertise. The authors gratefully acknowledge the support of compute resources provided by the Empire AI Consortium. The authors also acknowledge UFIT Research Computing (<http://www.rc.ufl.edu>) at the University of Florida, the Minnesota Supercomputing Institution (MSI) (<http://www.msi.umn.edu>) at the University of Minnesota, and resources provided by Drexel University through NSF Grant OAC-2320600, for providing computational resources and support that have contributed to the research results reported in this publication. The authors acknowledge funding from NSF Grant OAC-2311632. P.H. also acknowledges support by a grant from the Simons Foundation (839534, MT).

- 
- [1] L. Boeri, R. Hennig, P. Hirschfeld, G. Profeta, A. Sanna, E. Zurek, W. E. Pickett, M. Amsler, R. Dias, M. I. Eremets, C. Heil, R. J. Hemley, H. Liu, Y. Ma, C. Pierleoni, A. N. Kolmogorov, N. Rybin, D. Novoselov, V. Anisimov, A. R. Oganov, C. J. Pickard, T. Bi, R. Arita, I. Errea, C. Pellegrini, R. Requist, E. K. U. Gross, E. R. Margine, S. R. Xie, Y. Quan, A. Hire, L. Fanfarillo, G. R. Stewart, J. J. Hamlin, V. Stanev, R. S. Gonnelli, E. Piatto, D. Romanin, D. Daghero, and R. Valenti, *J. Phys.: Condens. Matter* **34**, 183002 (2022).
- [2] B. Gludovatz, A. Hohenwarter, D. Catoor, E. H. Chang, E. P. George, and R. O. Ritchie, *Science* **345**, 1153 (2014).
- [3] B. Gludovatz, A. Hohenwarter, K. V. S. Thurston, H. Bei, Z. Wu, E. P. George, and R. O. Ritchie, *Nat. Commun.* **7**, 10602 (2016).
- [4] E. P. George, D. Raabe, and R. O. Ritchie, *Nat. Rev. Mater.* **4**, 515 (2019).
- [5] D. Strmcnik, P. P. Lopes, B. Genorio, V. R. Stamenkovic, and N. M. Markovic, *Nano Energy Electrocatalysis*, **29**, 29 (2016).
- [6] Y. Nakaya and S. Furukawa, *Chem. Rev.* **123**, 5859 (2023).
- [7] C. Liu, F. Li, L.-P. Ma, and H.-M. Cheng, *Advanced Materials* **22**, E28 (2010).
- [8] G. J. Snyder and E. S. Toberer, *Nature Mater* **7**, 105 (2008).
- [9] B. Cantor, *Progress in Materials Science* **120**, 100754 (2021).
- [10] R. Potyrailo, K. Rajan, K. Stoewe, I. Takeuchi, B. Chisholm, and H. Lam, *ACS Comb. Sci.* **13**, 579 (2011).
- [11] W. F. Maier, *ACS Comb. Sci.* **21**, 437 (2019).
- [12] A. Jain, G. Hautier, C. Moore, S. Ong, C. Fischer, T. Mueller, K. Persson, and G. Ceder, *Comput. Mater. Sci.* **50**, 2295 (2011).
- [13] S. Curtarolo, G. L. W. Hart, M. B. Nardelli, N. Mingo, S. Sanvito, and O. Levy, *Nat. Mater.* **12**, 191 (2013).
- [14] G. Bergerhoff, R. Hundt, R. Sievers, and I. D. Brown, *J. Chem. Inf. Comput. Sci.* **23**, 66 (1983).
- [15] M. J. Mehl, D. Hicks, C. Toher, O. Levy, R. M. Hanson, G. Hart, and S. Curtarolo, *Comput. Mater. Sci.* **136**, S1 (2017).
- [16] B. Blaiszik, K. Chard, J. Pruyne, R. Ananthakrishnan, S. Tuecke, and I. Foster, *JOM* **68**, 2045 (2016).
- [17] J. A. Vita, E. G. Fuemmeler, A. Gupta, G. P. Wolfe, A. Q. Tao, R. S. Elliott, S. Martiniani, and E. B. Tadmor, *J. Chem. Phys.* **159**, 154802 (2023).
- [18] E. Fuemmeler, G. Wolfe, A. Gupta, J. A. Vita, E. B. Tadmor, and S. Martiniani, in *AI for Accelerated Materials Design-NeurIPS 2024* (2024).
- [19] S. Batzner, A. Musaelian, L. Sun, M. Geiger, J. P. Mailoa, M. Kornbluth, N. Molinari, T. E. Smidt, and B. Kozinsky, *Nature Communications* **13**, 2453 (2022).
- [20] I. Batatia, D. P. Kovacs, G. Simm, C. Ortner, and G. Csanyi, *Advances in Neural Information Processing Systems* **35**, 11423 (2022).
- [21] C. Chen and S. P. Ong, *Nature Computational Science* **2**, 718 (2022).
- [22] G. H. Booth, A. Grüneis, G. Kresse, and A. Alavi, *Nature* **493**, 365 (2013).
- [23] N. Zaki, H. Park, R. M. Osgood, A. J. Millis, and C. A. Marianetti, *Phys. Rev. B* **89**, 205427 (2014).
- [24] E. B. Isaacs and C. A. Marianetti, *Phys. Rev. B* **102**, 045146 (2020).
- [25] C. J. Pickard and R. J. Needs, *J. Phys.: Condens. Matter* **23**, 053201 (2011).
- [26] W. W. Tipton and R. G. Hennig, *Journal of Physics: Condensed Matter* **25**, 495401 (2013).
- [27] A. R. Oganov, C. J. Pickard, Q. Zhu, and R. J. Needs, *Nat Rev Mater* **4**, 331 (2019).
- [28] A. Merchant, S. Batzner, S. S. Schoenholz, M. Aykol, G. Cheon, and E. D. Cubuk, *Nature* **624**, 80 (2023).

- [29] T. Xie, X. Fu, O.-E. Ganea, R. Barzilay, and T. Jaakkola, Crystal Diffusion Variational Autoencoder for Periodic Material Generation (2022), arXiv:2110.06197 [cs].
- [30] R. Jiao, W. Huang, P. Lin, J. Han, P. Chen, Y. Lu, and Y. Liu, Crystal Structure Prediction by Joint Equivariant Diffusion (2023).
- [31] C. Zeni, R. Pinsler, D. Zügner, A. Fowler, M. Horton, X. Fu, Z. Wang, A. Shysheya, J. Crabbé, S. Ueda, R. Sordillo, L. Sun, J. Smith, B. Nguyen, H. Schulz, S. Lewis, C.-W. Huang, Z. Lu, Y. Zhou, H. Yang, H. Hao, J. Li, C. Yang, W. Li, R. Tomioka, and T. Xie, Nature 10.1038/s41586-025-08628-5 (2025).
- [32] B. K. Miller, R. T. Q. Chen, A. Sriram, and B. M. Wood, FlowMM: Generating Materials with Riemannian Flow Matching (2024), arXiv:2406.04713 [cond-mat, physics:physics, stat].
- [33] M. S. Albero, N. M. Boffi, and E. Vanden-Eijnden, Stochastic Interpolants: A Unifying Framework for Flows and Diffusions (2023), arXiv:2303.08797 [cond-mat].
- [34] J. Sohl-Dickstein, E. A. Weiss, N. Maheswaranathan, and S. Ganguli, Deep Unsupervised Learning using Nonequilibrium Thermodynamics (2015), arXiv:1503.03585 [cond-mat, q-bio, stat].
- [35] Y. Song, J. Sohl-Dickstein, D. P. Kingma, A. Kumar, S. Ermon, and B. Poole, Score-Based Generative Modeling through Stochastic Differential Equations (2021), arXiv:2011.13456 [cs].
- [36] C. Saharia, W. Chan, S. Saxena, L. Li, J. Whang, E. Denton, S. K. S. Ghasemipour, B. K. Ayan, S. S. Mahdavi, R. G. Lopes, T. Salimans, J. Ho, D. J. Fleet, and M. Norouzi, Photorealistic Text-to-Image Diffusion Models with Deep Language Understanding (2022), arXiv:2205.11487 [cs].
- [37] G. Corso, H. Stärk, B. Jing, R. Barzilay, and T. Jaakkola, DiffDock: Diffusion Steps, Twists, and Turns for Molecular Docking (2023), arXiv:2210.01776 [q-bio].
- [38] Y. Lipman, R. T. Q. Chen, H. Ben-Hamu, M. Nickel, and M. Le, Flow Matching for Generative Modeling (2023), arXiv:2210.02747 [cs, stat].
- [39] A. Tong, K. Fatras, N. Malkin, G. Huguet, Y. Zhang, J. Rector-Brooks, G. Wolf, and Y. Bengio, Improving and generalizing flow-based generative models with minibatch optimal transport (2024), arXiv:2302.00482.
- [40] R. T. Q. Chen and Y. Lipman, Flow Matching on General Geometries (2024), arXiv:2302.03660 [cs, stat].
- [41] I. Gat, T. Remez, N. Shaul, F. Kreuk, R. T. Q. Chen, G. Synnaeve, Y. Adi, and Y. Lipman, Discrete Flow Matching (2024), arXiv:2407.15595 [cs].
- [42] A. Campbell, J. Yim, R. Barzilay, T. Rainforth, and T. Jaakkola, Generative Flows on Discrete State-Spaces: Enabling Multimodal Flows with Applications to Protein Co-Design (2024), arXiv:2402.04997 [cs, q-bio, stat].
- [43] D. W. Davies, K. T. Butler, A. J. Jackson, J. M. Skelton, K. Morita, and A. Walsh, Journal of Open Source Software 4, 1361 (2019).
- [44] M. S. Albero, M. Goldstein, N. M. Boffi, R. Ranganath, and E. Vanden-Eijnden, Stochastic interpolants with data-dependent couplings (2024), arXiv:2310.03725 [cs, stat].
- [45] J. Yim, A. Campbell, A. Y. K. Foong, M. Gastegger, J. Jiménez-Luna, S. Lewis, V. G. Satorras, B. S. Veeling, R. Barzilay, T. Jaakkola, and F. Noé, Fast protein backbone generation with SE(3) flow matching (2023), arXiv:2310.05297.
- [46] A. J. Bose, T. Akhound-Sadegh, G. Huguet, K. Fatras, J. Rector-Brooks, C.-H. Liu, A. C. Nica, M. Korablyov, M. Bronstein, and A. Tong, SE(3)-Stochastic Flow Matching for Protein Backbone Generation (2024), arXiv:2310.02391.
- [47] V. G. Satorras, E. Hoogetboom, and M. Welling, in *Proceedings of the 38th International Conference on Machine Learning*, Proceedings of Machine Learning Research, Vol. 139, edited by M. Meila and T. Zhang (PMLR, 2021) pp. 9323–9332.
- [48] M. AI4Science, A. Hernandez-Garcia, A. Duval, A. Volokhova, Y. Bengio, D. Sharma, P. L. Carrier, Y. Benabed, M. Koziarski, and V. Schmidt, Crystal-GFN: Sampling crystals with desirable properties and constraints (2023), arXiv:2310.04925 [cs].
- [49] Z. Cao, X. Luo, J. Lv, and L. Wang, Space Group Informed Transformer for Crystalline Materials Generation (2024).
- [50] R. Zhu, W. Nong, S. Yamazaki, and K. Hippalgaonkar, WyCryst: Wyckoff Inorganic Crystal Generator Framework (2024), arXiv:2311.17916.
- [51] N. Kazeev, R. Zhu, I. Romanov, A. E. Ustyuzhanin, S. Yamazaki, W. Nong, and K. Hippalgaonkar, in *AI for Accelerated Materials Design - NeurIPS 2024* (2024).
- [52] R. Jiao, W. Huang, Y. Liu, D. Zhao, and Y. Liu, Space Group Constrained Crystal Generation (2024), arXiv:2402.03992 [cond-mat].
- [53] MatterGen, Mattergen, Microsoft (2025).
- [54] I. E. Castelli, D. D. Landis, K. S. Thygesen, S. Dahl, I. Chorkendorff, T. F. Jaramillo, and K. W. Jacobsen, Energy & Environmental Science 5, 9034 (2012).
- [55] A. Jain, S. P. Ong, G. Hautier, W. Chen, W. D. Richards, S. Dacek, S. Cholia, D. Gunter, D. Skinner, G. Ceder, and K. A. Persson, APL Materials 1, 011002 (2013).
- [56] S. G. Baird, H. M. Sayeed, J. Montoya, and T. D. Sparks, Journal of Open Source Software 9, 5618 (2024).
- [57] J. Schmidt, N. Hoffmann, H.-C. Wang, P. Borlido, P. J. M. A. Carriço, T. F. T. Cerqueira, S. Botti, and M. A. L. Marques, Large-scale machine-learning-assisted exploration of the whole materials space (2022), arXiv:2210.00579 [cond-mat].
- [58] J. Schmidt, H.-C. Wang, T. F. T. Cerqueira, S. Botti, and M. A. L. Marques, Scientific Data 9, 64 (2022).
- [59] C. J. Pickard, Airss data for carbon at 10gpa and the c+n+h+o system at 1gpa (2020).
- [60] S. P. Ong, W. D. Richards, A. Jain, G. Hautier, M. Kocher, S. Cholia, D. Gunter, V. L. Chevrier, K. A. Persson, and G. Ceder, Computational Materials Science 68, 314 (2013).
- [61] H. Yang, C. Hu, Y. Zhou, X. Liu, Y. Shi, J. Li, G. Li, Z. Chen, S. Chen, C. Zeni, M. Horton, R. Pinsler, A. Fowler, D. Zügner, T. Xie, J. Smith, L. Sun, Q. Wang, L. Kong, C. Liu, H. Hao, and Z. Lu, MatterSim: A Deep Learning Atomistic Model Across Elements, Temperatures and Pressures (2024), arXiv:2405.04967.
- [62] R. Liaw, E. Liang, R. Nishihara, P. Moritz, J. E. Gonzalez, and I. Stoica, arXiv preprint arXiv:1807.05118 (2018).
- [63] J. Bergstra, D. Yamins, and D. D. Cox, TProc. of the 30th International Conference on Machine Learning (ICML 2013), pp. I (2013).
- [64] R. W. Grosse-Kunstleve, N. K. Sauter, and P. D. Adams, Acta Cryst A 60, 1 (2004).
- [65] A. Hjorth Larsen, J. Jørgen Mortensen, J. Blomqvist, I. E. Castelli, R. Christensen, M. Dulak, J. Friis,

M. N. Groves, B. Hammer, C. Hargus, E. D. Hermes, P. C. Jennings, P. Bjerre Jensen, J. Kermode, J. R. Kitchin, E. Leonhard Kolsbjerg, J. Kubal, K. Kaasbjerg, S. Lysgaard, J. Bergmann Maronsson, T. Maxson, T. Olsen, L. Pastewka, A. Peterson, C. Rostgaard, J. Schiøtz, O. Schütt, M. Strange, K. S. Thygesen,

T. Vegge, L. Vilhelmsen, M. Walter, Z. Zeng, and K. W. Jacobsen, *J. Phys.: Condens. Matter* **29**, 273002 (2017).  
 [66] A. Togo, K. Shinohara, and I. Tanaka, Spglib: A software library for crystal symmetry search (2024), arXiv:1808.01590 [cond-mat].

## Appendix A: Implementation details of stochastic interpolants

### 1. OMG Framework

Figures 4 and 5 summarize the training and the integration pipeline of the OMG framework, respectively. Depending on the specific task, there are several stochastic interpolants at once. For CSP, one stochastic interpolant considers lattice vectors  $\mathbf{L}$ , and another one considers fractional coordinates  $\mathbf{X}$ . The model output of CSPNet (see Appendix B 1) depends on the full structural representation  $\{\mathbf{A}, \mathbf{X}, \mathbf{L}\}$  and time  $t$ , where  $\mathbf{A}$  are the atomic species. For the DNG task, we additionally use discrete flow matching for the atomic species  $\mathbf{A}$  [42].

During the numerical integration in the CSP task,  $\mathbf{X}$  and  $\mathbf{L}$  are integrated jointly while  $\mathbf{A}$  is fixed. For DNG,  $\mathbf{A}$  is evolved according to discrete flow matching [42] (see Appendix A 5). For the SDE sampling scheme in Fig. 5, one chooses a time-dependent noise  $\varepsilon(t)$  that only appears during integration and not during training. Also,  $\gamma(t)$  has to be unequal zero in order to prevent the divergence in  $1/\gamma(t)$ . However, since  $\gamma(t)$  necessarily vanishes at times  $t = 0$  and  $t = 1$  (see Appendix A 2), one should choose a time-varying  $\varepsilon(t)$  that vanishes near these endpoints [33].

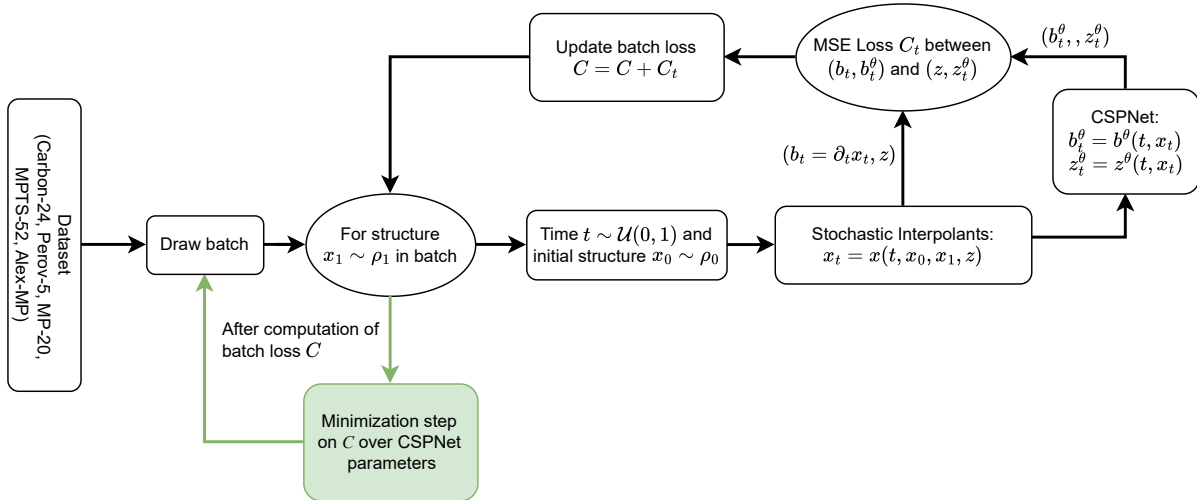


FIG. 4. Training pipeline of the OMG framework: A batch of structures is drawn from a dataset with target distribution  $\rho_1$ . Every structure  $x_1 \sim \rho_1$  is connected with a structure  $x_0$  from the base distribution  $\rho_0$  with stochastic interpolants that yield the interpolated structure  $x_t = x(t, x_0, x_1, z)$  and the drift  $b_t = \partial_t x_t$  at time  $t \sim \mathcal{U}(0, 1)$ , possibly using a random variable  $z \sim \mathcal{N}(0, \mathbf{I})$ . The model CSPNet predicts  $b_t^\theta = b^\theta(t, x_t)$  and  $z_t^\theta = z^\theta(t, x_t)$  and its parameters are minimized based on the MSE losses in Eqs 2 and 3.

### 2. Interpolant choice

We are concerned with interpolants with the form specified in Eq. 1. Here, the following conditions must be met [33]:

$$\alpha(0) = \beta(1) = 1, \quad \alpha(1) = \beta(0) = \gamma(0) = \gamma(1) = 0, \quad \gamma(t) > 0 \forall t \in (0, 1) \quad (\text{A1})$$

Under these constraints, the form of the SI is relatively flexible, and many different interpolants can be defined (see Tab. V). An additional advantage of SI is that the base distribution can be arbitrary as in CFM [39]. We find that particular forms of the stochastic interpolants result in better performance than others. To add to the flexibility of the

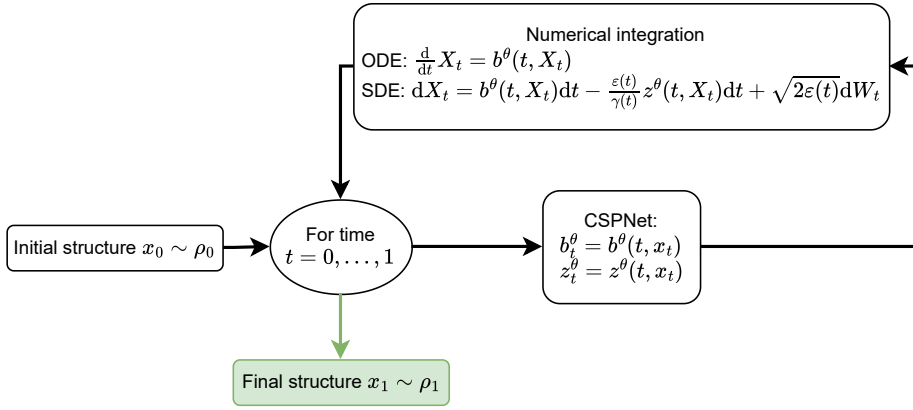


FIG. 5. Numerical integration pipeline of the OMG framework: An initial structure  $x_0$  from the base distribution  $\rho_0$  is numerically integrated following either an ODE or an SDE based on the model predictions  $b_i^\theta$  and  $z_i^\theta$ . For an SDE, one can choose a noise  $\varepsilon(t)$  during integration.

TABLE V. SI parameters from Albergo *et al.* [33].

Stochastic Interpolant	$\alpha(t)$	$\beta(t)$	$\gamma(t)$
linear	$1 - t$	$t$	$\sqrt{at(1-t)}$
Arbitrary $\rho_0$ trig	$\cos \frac{\pi}{2}t$	$\sin \frac{\pi}{2}t$	$\sqrt{at(1-t)}$
enc-dec	$\cos^2(\pi t)1_{[0, \frac{1}{2})}(t)$	$\cos^2(\pi t)1_{(\frac{1}{2}, 1]}(t)$	$\sin^2(\pi t)$
linear	$1 - t$	$t$	0
Gaussian $\rho_0$ trig	$\cos \frac{\pi}{2}t$	$\sin \frac{\pi}{2}t$	0
SBD	$\sqrt{1-t^2}$	$t$	0
Mirror	0	1	$\sqrt{at(1-t)}$

SI framework, ODE or SDE integration can be used to sample from a trained SI model. We thoroughly explore the use of both of these techniques to investigate the performance of SI on different elements of the crystal unit cell.

### 3. Antithetic sampling

As shown by Albergo *et al.* [33], inspection of possible  $\gamma$  terms and of Eq. 2 reveals that the loss function can become unstable around  $t = 0$  and  $t = 1$ . To account for this, we implement antithetic sampling. This requires to compute the loss at both  $x^+$  and  $x^-$  where:

$$x^+(t, x_0, x_1, z) = \alpha(t)x_0 + \beta(t)x_1 + \gamma(t)z, \quad (\text{A2})$$

$$x^-(t, x_0, x_1, z) = \alpha(t)x_0 + \beta(t)x_1 - \gamma(t)z. \quad (\text{A3})$$

### 4. Interpolation with periodic boundary conditions

We show in Fig. 6 how we implement periodic versions of interpolants in order to represent fractional coordinates in a unit cell with periodic boundary conditions. We emphasize that this procedure is important not only for the choice of interpolant, but also for the addition of the latent variable  $\gamma(t)z$  which also moves the interpolation trajectory away from the geodesic.

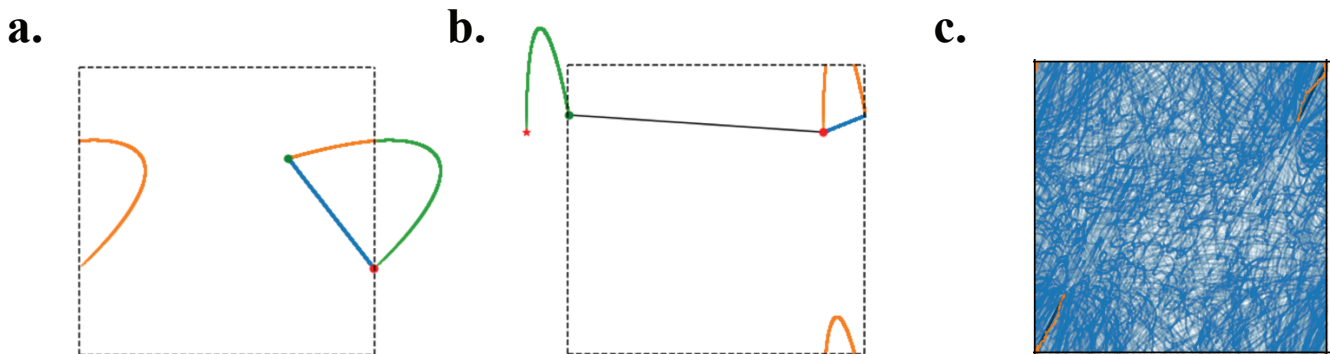


FIG. 6. Extending interpolants to incorporate periodic boundary conditions. **(a–b)** The path for a score based diffusion interpolant is calculated by first computing the shortest-path geodesic (blue) between the initial (green dot) and final positions (red dot). Next, the path of the interpolant moving the final position outside the bounding box is computed (green), and finally the path is wrapped back into the bounding box to produce the interpolant trajectory (orange). **(c)** The effect of adding a latent variable to any interpolant must be handled similarly to calculating the path of a non-linear interpolant. For a linear interpolant with a nonzero  $\gamma$ , we show samples of possible paths (blue) and their averaged path (orange) which collapses onto the path of the linear interpolant.

## 5. DFM Details

DFM allows for generative modeling of discrete sequences of tokens while respecting the discrete nature of the design space. As discussed, a parameterized neural network  $p_{1|t}^\theta(x_1|x_t)$  is learned, which attempts to predict the final sequence from the current sequence. Borrowing from Campbell *et al.* [42], we choose a conditional rate matrix  $R_t(x_t, i|x_1)$  generating the conditional flow  $p_{t|1}(x_t|x_1)$  of the form:

$$R_t(x_t, i|x_1) = \frac{\text{ReLU}(\partial_t p_{t|1}(i|x_1) - \partial_t p_{t|1}(x_t|x_1))}{S \cdot p_{t|1}(x_t|x_1)}, \quad (\text{A4})$$

where  $S$  is the number of possible tokens a sequence element can take on. This conditional rate matrix can be modified by including a term that introduces stochasticity in the form of a detailed balance rate matrix  $R_t^{DB}$  by writing  $R_t^\eta = R_t + \eta R_t^{DB}$ . Here, [42]:

$$R_t^{DB}(i, j|x_1) = \eta \delta\{i, x_1\} \delta\{j, M\} + \frac{\eta t}{1-t} \delta\{i, M\} \delta\{j, x_1\}, \quad (\text{A5})$$

where  $M$  is the masking token. The parameter  $\eta \in \mathbb{R}^+$  represents the level of stochasticity that only appears during generation.

During generation, our objective is to compute  $R_t^\theta(x_t, i)$  based on the learned distribution  $p_{1|t}^\theta(x_1|x_t)$ . Formally, we have

$$R_t^\theta(x_t, i) = \mathbb{E}_{p_{1|t}^\theta(x_1|x_t)} [R_t^\eta(x_t, i|x_1)] \quad (\text{A6})$$

In practice, Campbell *et al.* [42] show that we need not compute a full expectation, but rather, simply draw  $x_1 \sim p_{1|t}^\theta(x_1|x_t)$ , evaluate the conditional rate matrix, and perform an update of  $x_t$  to  $x_{t+\Delta t}$  with discrete time step  $\Delta t$  directly from this by sampling  $x_{t+\Delta t}$  according to

$$p_{t+\Delta t|t}(x_{t+\Delta t}|x_1, x_t) = \delta\{x_t, x_{t+\Delta t}\} + R_t^\eta(x_t, i|x_1) \Delta t. \quad (\text{A7})$$

## 6. Permuting particle order to achieve minimum interpolated distance

We experiment with biasing the initial distribution such that we learn interpolant paths that are shorter on average than independently chosen  $(x_0, x_1)$  pairs. Formally, our coupling is conditional on the sampled  $(x_0, x_1)$  and is defined as

$$\arg \min_p \sum_i d(p(x_0^i), x_1^i). \quad (\text{A8})$$

Here,  $d(\cdot, \cdot)$  is a distance metric which we define on a periodic manifold in fractional-coordinate space (*i.e.*, a four-dimensional torus) and  $p$  is some permutation function that permutes the discrete indices  $i$ . Under this coupling, we still sample  $(x_0, x_1)$  independently but then bias the sampled  $x_0$  to travel the minimum permutational distance necessary to reach the target structure. We show the performance of this method in Tab. IV for our DNG models.

## Appendix B: Model architecture

### 1. Graph neural network

We implement a message-passing GNN with CSPNet introduced in Jiao *et al.* [30]:

$$\mathbf{h}_{(0)}^i = \phi_{\mathbf{h}_{(0)}}(\mathbf{a}^i) \quad (\text{B1})$$

$$\mathbf{m}_{(s)}^{ij} = \varphi_m \left( \mathbf{h}_{s-1}^i, \mathbf{h}_{s-1}^j, \mathbf{l}, \text{SinusoidalEmbedding}(\mathbf{x}^j - \mathbf{x}^i) \right) \quad (\text{B2})$$

$$\mathbf{m}_{(s)}^i = \sum_{j=1}^N \mathbf{m}_{(s)}^{ij} \quad (\text{B3})$$

$$\mathbf{h}_{(s)}^i = \mathbf{h}_{(s-1)}^i + \varphi_h(\mathbf{h}_{(s-1)}, \mathbf{m}_{(s)}^i) \quad (\text{B4})$$

$$\mathbf{b}_{\mathbf{x}} = \varphi_{\mathbf{x}} \left( \mathbf{h}_{(\max s)}^i \right) \quad (\text{B5})$$

$$\mathbf{b}_{\mathbf{l}} = \varphi_{\mathbf{l}} \left( \frac{1}{n} \sum_{i=1}^n \mathbf{h}_{(\max s)}^i \right) \quad (\text{B6})$$

Here, node embeddings,  $\mathbf{h}$ , are initialized as a function of the atom types,  $\mathbf{a}$ . Embeddings are then updated by a message passing scheme through a series of graph convolution layers. Messages are computed with a parameterized neural network,  $\varphi_m$ . Messages are computed from neighboring node embeddings as well as information about the lattice,  $\mathbf{l}$ , and distance between the fractional coordinates  $\mathbf{x}$ .

For the CFP model that should only prediction compositions, we simply remove the input of the lattice  $\mathbf{l}$  and the fractional coordinates  $\mathbf{x}$  from the computation of the message in Eq. B2. This ensures that the output  $p_{1|t}^\theta(\mathbf{a}_1|x_t)$  of CSPNet for the composition does not depend on lattice vectors or fractional coordinates, while preserving permutational equivariance.

### 2. Loss function

With Equations 2, 3, and 4, we can construct a loss function for the modeling of our joint distribution of interest,

$$\begin{aligned} \mathcal{L}(\theta) = & \mathbb{E}_{t,z,x_0,x_1} [ \\ & \lambda_{\mathbf{x},b} [|b_{\mathbf{x}}^\theta(t, x_t)|^2 - 2\partial_t x(t, x_0, x_1, z) \cdot b_{\mathbf{x}}^\theta(t, x_t)] + \lambda_{\mathbf{x},z} [|z_{\mathbf{x}}^\theta(t, x_t)|^2 - 2z_{\mathbf{x}}^\theta(t, x_t) \cdot z] \\ & + \lambda_{\mathbf{l},b} [|b_{\mathbf{l}}^\theta(t, x_t)|^2 - 2\partial_t x(t, x_0, x_1, z) \cdot b_{\mathbf{l}}^\theta(t, x_t)] + \lambda_{\mathbf{l},z} [|z_{\mathbf{l}}^\theta(t, x_t)|^2 - 2z_{\mathbf{l}}^\theta(t, x_t) \cdot z] \\ & + \lambda_{\mathbf{a}} [\log p_{1|t}^\theta(\mathbf{a}_1|x_t)] ]. \end{aligned} \quad (\text{B7})$$

where the  $\lambda$  terms correspond to the relative weights of each term in the loss function. These weighting factors are hyperparameters that are included in our hyperparameter sweep.

### 3. Hyperparameter optimization

Hyperparameter optimization was performed using the `Ray Tune` package [62] in conjunction with the `HyperOpt` Python library [63] for Bayesian optimization. The tuned hyperparameters include both those relevant during training—the relative losses  $\lambda$ , the choice of stochastic interpolant for the atomic coordinates, the parameters for chosen  $\gamma(t)$  (if necessary), the sampling scheme, the usage of data-dependent coupling, the batch size, and the learning rate—and during inference—the number of integration steps, the choice of the noises  $\varepsilon(t)$  and  $\eta$ , and the magnitude of the velocity annealing parameter  $s$  for both lattice vectors and atomic coordinates. Additionally, `OMG` provides the option to use the Niggli-reduced primitive cell [64, 65] for training, though we did not include this in the hyperparameter tuning as preliminary tests suggested no difference in model performance on the *MP-20* dataset.

## Appendix C: Metrics for evaluating learned models

### 1. Match rate and RMSE

We include here a discussion on the tradeoff between match rate and RMSE, as we noticed this most strongly influences the *perov-5* dataset. We show in Fig. 7 how different interpolants for the atomic coordinates (trigonometric vs. linear) learn to match structures differently. For the linear case (which has a depressed match rate) the change in matching tolerance makes little difference; for the trigonometric interpolant it makes a far more significant difference and leads to a much higher match rate, suggesting that the trigonometric interpolant learns structures more reliably but less accurately.

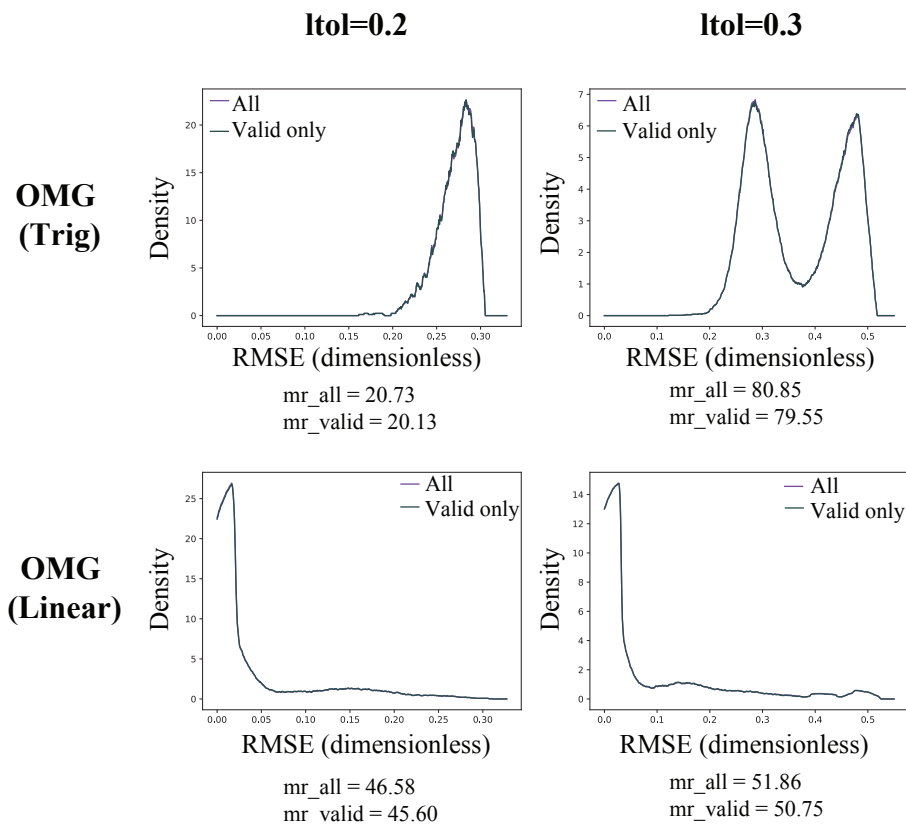


FIG. 7. We show here the effect of making matching more difficult by decreasing the length tolerance used by `pymatgen`'s `StructureMatcher`. We plot the density of the normalized RMSE distributions from CSP models trained on the *perov-5* dataset. We note that the curves for all generated structures and only valid generated structures overlap significantly.

## 2. Validity metrics

We noted that for the compositional validity metric, the version of the SMACT software [43] changed the computed values by several percent. This impacts both the match rate (when filtered by valid structures) as well as the reported DNG compositional validity output. As such, all values for all models were recomputed with the most up-to-date version (3.0) of the SMACT software.

## 3. Calculation of S.U.N. rates

Evaluation of DNG structures was performed using scripts provided by the developers of MatterGen [53]. A total of 10,000 structures were generated from each of OMG, DiffCSP, and FlowMM. These structures were then filtered to remove any that contained elements not supported by the MatterSim potential (version `MatterSim-v1.0.0-1M`) or the reference convex hull. These included heavy elements with atomic numbers  $>89$ , radioactive elements, and the noble gases (specifically: ‘Ac’, ‘U’, ‘Th’, ‘Ne’, ‘Tc’, ‘Kr’, ‘Pu’, ‘Np’, ‘Xe’, ‘Pm’, ‘He’, ‘Pa’). Stability and novelty were computed with respect to the default dataset provided by MatterGen which contains 845,997 structures from the *MP-20* [29, 55] and *Alexandria* [57, 58] datasets. This provides a more challenging reference for computing novelty as each model was trained only on the  $\sim 27,000$  structures from the *MP-20* training set.

## 4. Structural and stability analysis of generated structures

In Fig. 8, we show the distribution of computed energies above the convex hull across various OMG models, showing best stability of generated structures for linear, encoder-decoder, trigonometric, and score-based diffusion (SBD) positional interpolants.

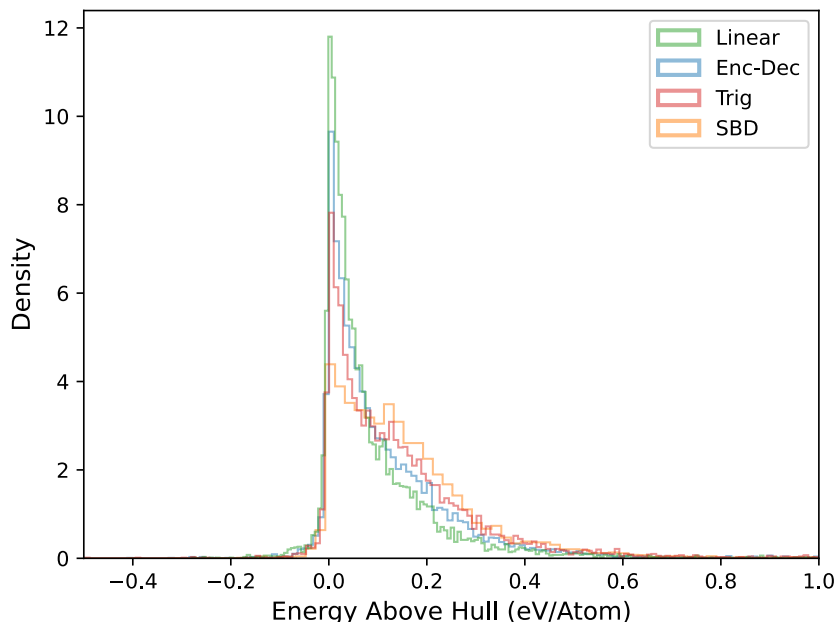


FIG. 8. Histogram of the computed energies above the convex hull for structures generated by four OMG DNG models trained using joint evolution for cell, coordinates, and species. We show that the linear and encoder-decoder positional interpolants are effective at generating more structures close to the convex hull. See Appendix C 3 for calculation details.

By evaluating the distribution of  $N$ -ary structures (Fig. 9), the distribution of average coordination numbers (both by structure in Fig. 10 and by species in Fig. 11), as well as distribution of crystal systems (Fig. 12) which are related to a structure’s Bravais lattice, we provide qualitative analysis for model performance. Space groups (and thus crystal system) were determined using the `spglib` software [66]. Generally, OMG and DiffCSP showed the best performance

in matching the distribution of average coordination number for each structure, particularly for high-coordinated structures. DiffCSP performed most poorly among the four models on the  $N$ -ary structural similarity. The average coordination number for species were best-matched by the two OMG models, and of these two the linear interpolant generated the distribution of crystal systems best.

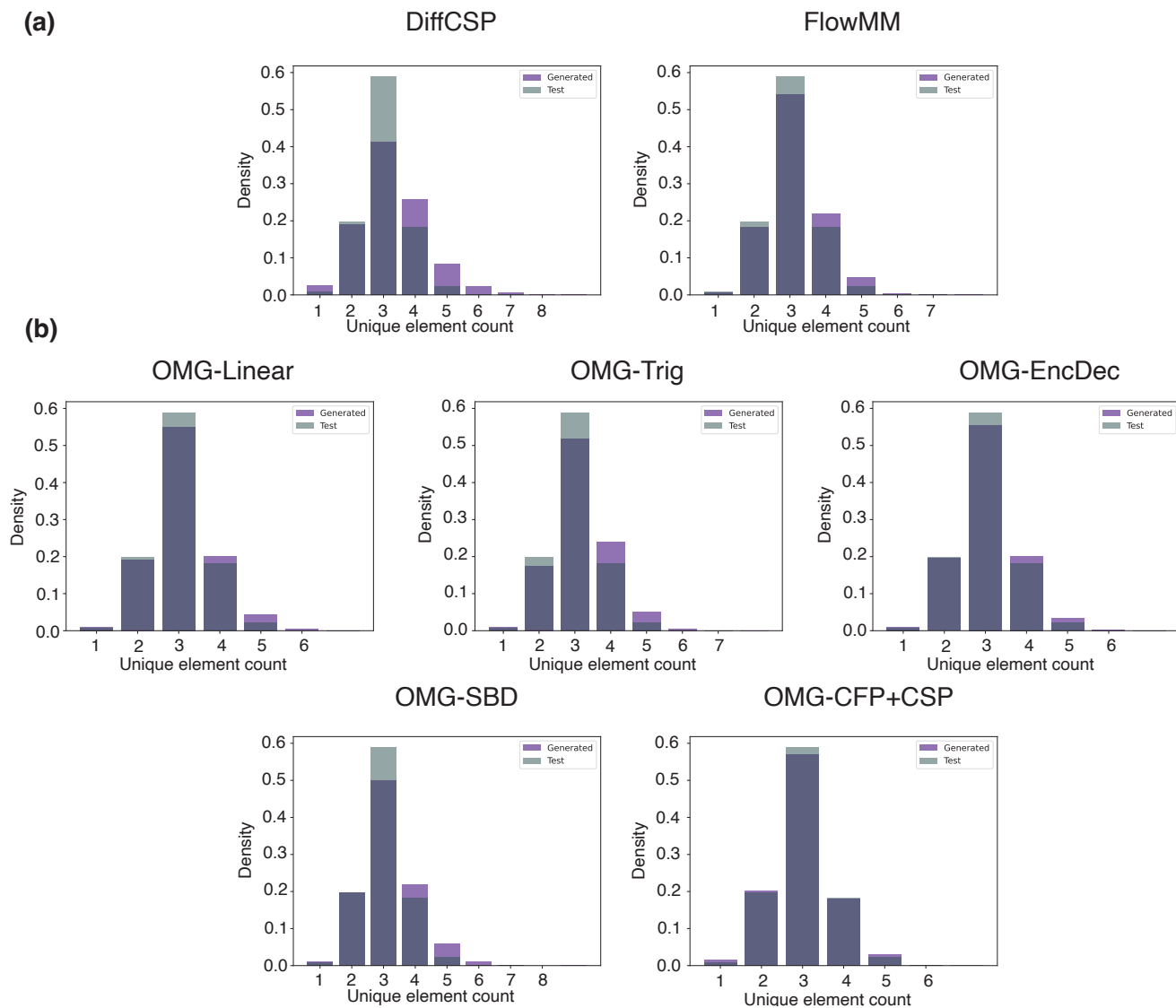


FIG. 9. Qualitative performance of the distribution of  $N$ -ary crystals for **(a)** Non-OMG models and **(b)** OMG models across structural benchmarks computed on generated structures and test set structures from the *MP-20* dataset.

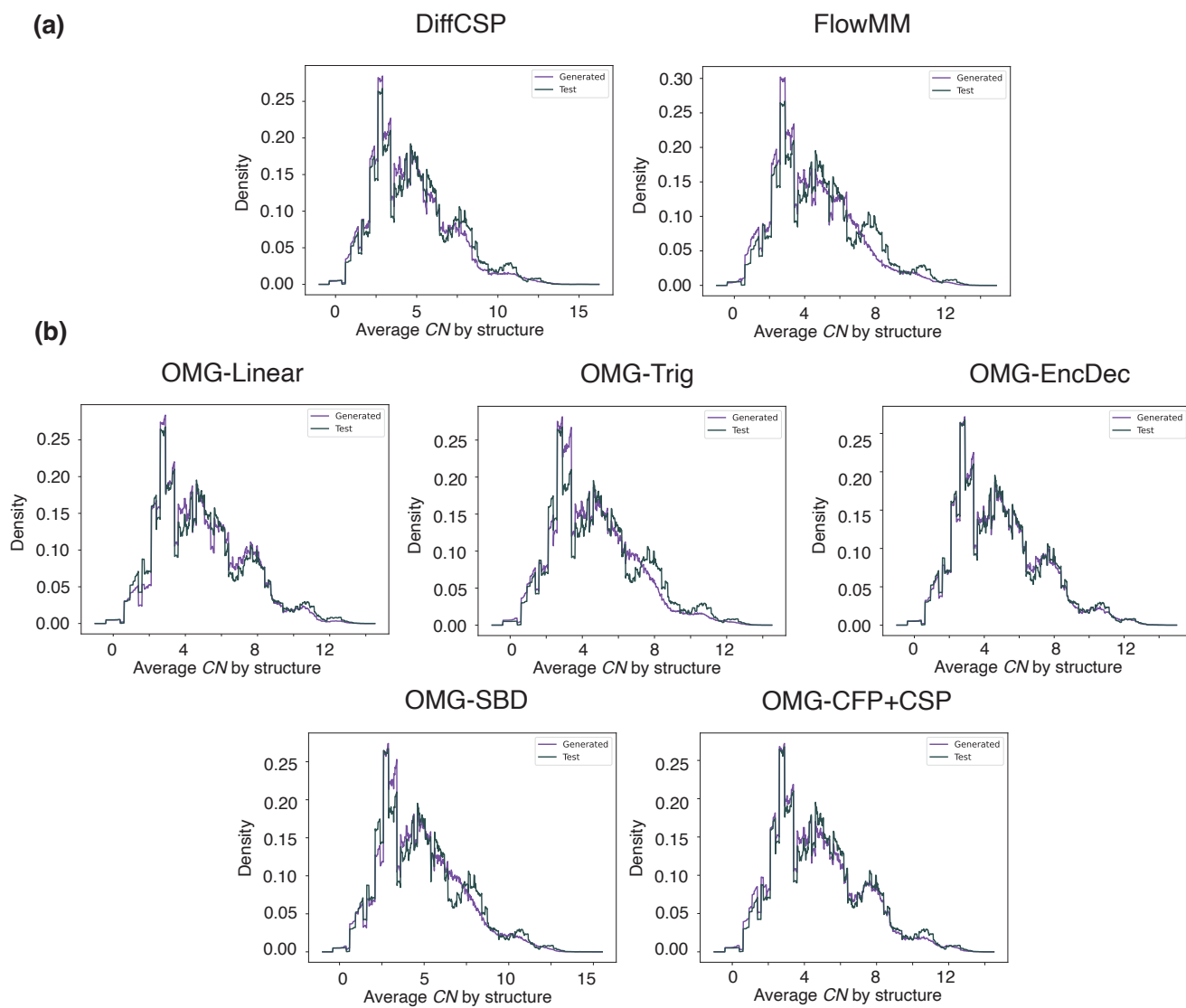


FIG. 10. Qualitative performance of the distribution of average coordination number by structure for **(a)** Non-OMG models and **(b)** OMG models across structural benchmarks computed on generated structures and test set structures from the *MP-20* dataset.

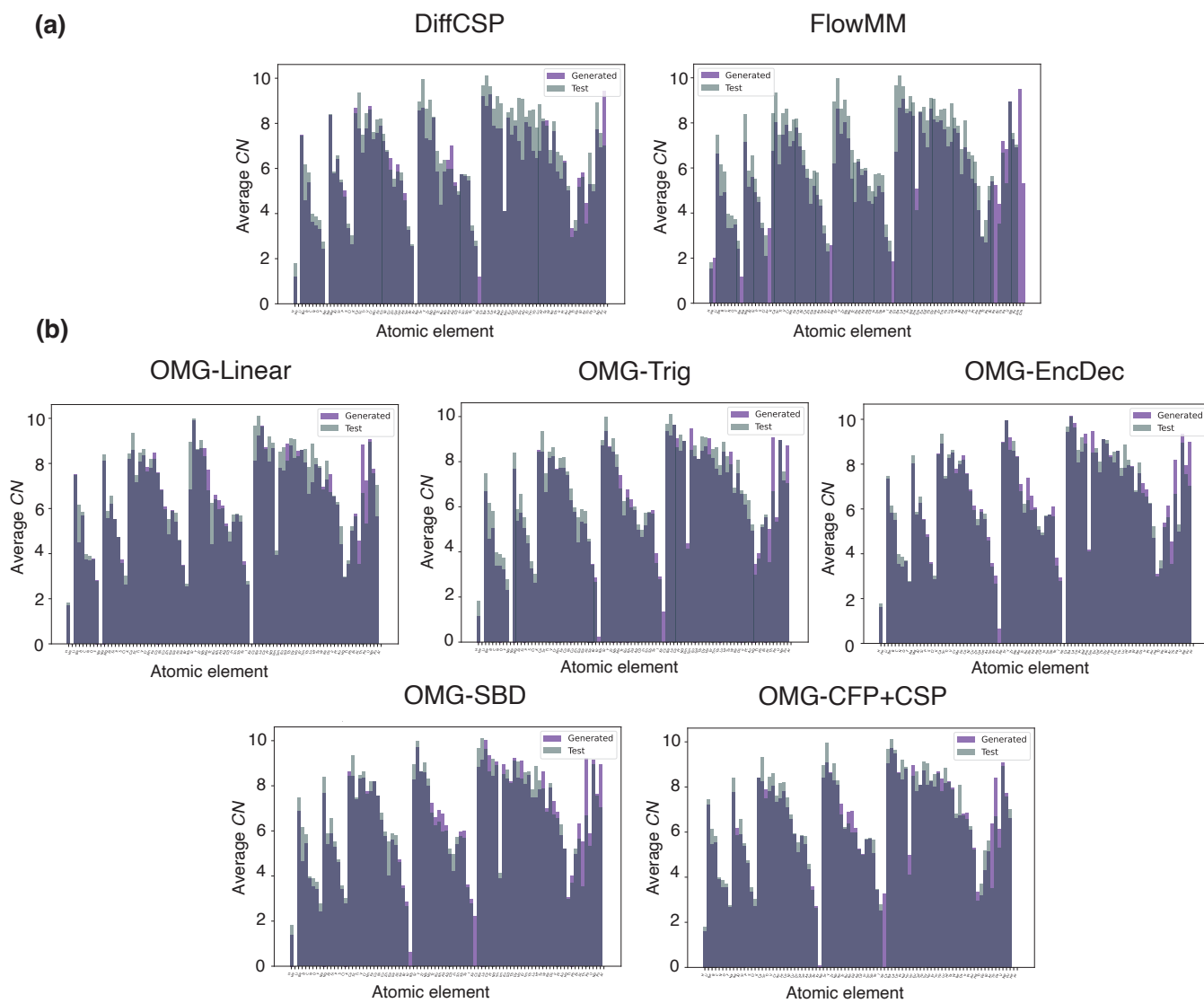


FIG. 11. Qualitative performance of the distribution of average coordination number by species (listed left to right in order of atomic number) for **(a)** Non-OMG models and **(b)** OMG models across structural benchmarks computed on generated structures and test set structures from the *MP-20* dataset.

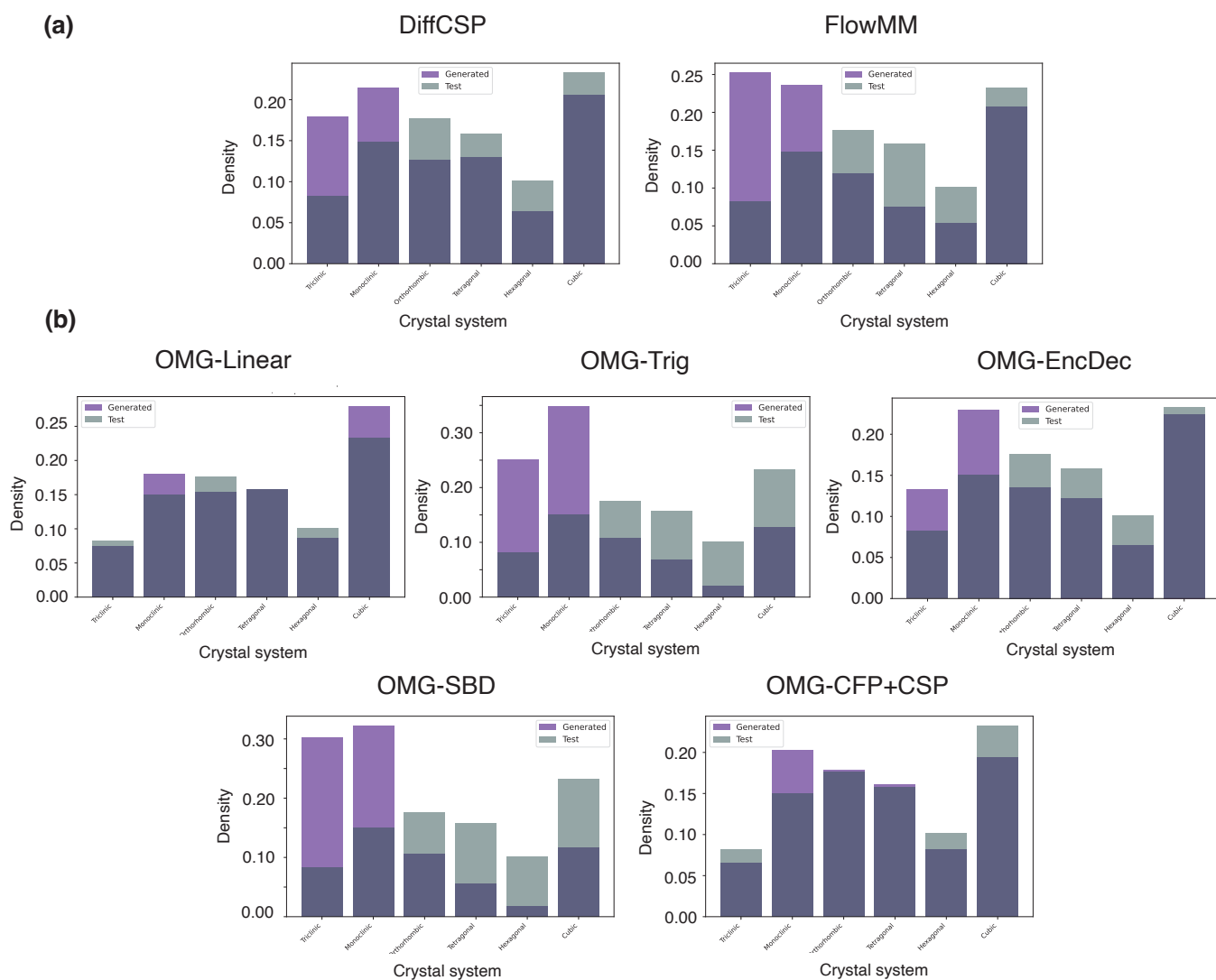


FIG. 12. Qualitative performance of the distribution of crystal system by structure for **(a)** Non-OMG models and **(b)** OMG models across structural benchmarks computed on generated structures and test set structures from the *MP-20* dataset.